



18 **ABSTRACT**

19 The global radiative effect of brown carbon (BrC) remains highly uncertain. BrC's  
20 photobleaching, which significantly affects its radiative effect, has been still poorly constrained.  
21 This study investigates and compares photobleaching rates of laboratory-synthesized secondary  
22 BrC (aq-BrC), biomass burning-derived BrC (b-BrC), and ambient PM<sub>2.5</sub>-derived BrC (p-BrC) to  
23 illustrate the variability in BrC photobleaching kinetics from different types of BrC reported in  
24 prior studies. Our results reveal a source dependence in BrC photobleaching rates. The highest  
25 photobleaching rate constant ( $k_{BrC}$ ) is observed for aq-BrC ( $1.13 \pm 0.08 \text{ h}^{-1}$ ), followed by p-BrC  
26 ( $0.12 \pm 0.02 \text{ h}^{-1}$ ) and b-BrC ( $0.05 \pm 0.01 \text{ h}^{-1}$ ), indicating the stable light-absorption capacity of b-  
27 BrC in the atmosphere. Integration of these rate constants with data derived from previous studies  
28 highlighted the differences in photobleaching behaviors among BrC from different sources. The  
29 OH oxidation of imidazole-2-carboxaldehyde (2-IC) and methylglyoxal oligomers, nitrophenols  
30 (including phenols), and lignin derivatives governs the photobleaching of aq-BrC, p-BrC, and b-  
31 BrC, respectively. The high  $k_{BrC}$  of aq-BrC is attributed to the high reactivity of the chain structures  
32 in 2-IC and methylglyoxal oligomers. In contrast, the highly conjugated structures of lignin  
33 derivatives in b-BrC impart stability against OH oxidation, resulting in a low  $k_{BrC}$ . Our findings  
34 reveal the significant differences in the photobleaching behavior of BrC originated from different  
35 sources, underscoring the crucial need to account for source differences in assessments of BrC's  
36 global radiative forcing effect.

37

## 38 **1. Introduction**

39 Brown carbon (BrC) is a significant contributor to atmospheric warming (Saleh, 2020; Chung et al., 2012;  
40 Brown et al., 2021) and Earth's radiative budget (Bond, 2001; Kirchstetter et al., 2004; Wang et al., 2018; Wang  
41 et al., 2022) due to its ultraviolet-visible (UV-Vis) light absorption. The BrC's direct radiative effect (DRE),  
42 accounting for 20%–40% of total DRE caused by light-absorbing carbonaceous aerosols (Heald et al., 2014; Jo  
43 et al., 2016; Saleh et al., 2015; Wang et al., 2018; Wang et al., 2014), remains highly uncertainty. BrC with global  
44 average DRE values varying from +0.03 to +0.57 W/m<sup>2</sup> is considered as the least understood warming agents in  
45 the atmosphere (Zhang et al., 2020; Zeng et al., 2020; Corr et al., 2012).

46 BrC comprises abundant chemically reactive species that react readily with atmospheric reactive gases and  
47 radicals (Aiona et al., 2017; Fleming et al., 2020; Hems et al., 2021; Liu et al., 2020), modifying its light-  
48 absorption properties. Both laboratory experiments (Borduas-Dedekind et al., 2019; Fleming et al., 2019; Hems  
49 and Abbatt, 2018; Hems et al., 2020; Schnitzler and Abbatt, 2018; Schnitzler et al., 2022) and field campaigns  
50 (Dasari et al., 2019; Qiu et al., 2024; Wang et al., 2014; Xu et al., 2024; Zeng et al., 2020) consistently found  
51 that BrC's photochemical aging process reduced its mass absorption coefficient (MAC), which is also known as  
52 photobleaching. In current models, the evaluation of BrC photobleaching on its radiative forcing effect mainly  
53 depends on the temporal decline in BrC's light-absorption capacity (Schnitzler et al., 2022; Wang et al., 2018;  
54 Xu et al., 2024), i.e., the photobleaching rate, which is substantial variability across different laboratory  
55 experiments and field observations. Notably, BrC generated from aqueous-phase reactions often exhibits  
56 negligible absorbance in the UV-Vis range after less than 2 hours of radiation (Aiona et al., 2017). Field  
57 observations reveal that atmospheric BrC undergoes a MAC reduction exceeding 60% after 1 day of sunlight  
58 exposure (Müller et al., 2023; Qiu et al., 2024). In comparison, over the same 1 day of solar radiation, the  
59 reduction in the MAC of BrC derived from biomass burning is much lower than atmospheric BrC (Fan et al.,  
60 2019; Fleming et al., 2020; Müller et al., 2023; Wong et al., 2019). Accurately determining BrC's photobleaching  
61 rate is paramount for quantifying the impact of BrC photobleaching on its radiative forcing effect in models.

62 Furthermore, BrC's chemical composition fundamentally governs its photochemical reactivity (Hems et al.,  
63 2021; Hems and Abbatt, 2018; Dalton and Nizkorodov, 2021; Liu et al., 2025), thereby modulating its  
64 photobleaching rate. However, the relationship between changes in BrC's molecular composition and light  
65 absorption properties during the photobleaching is still poorly constrained. This knowledge gap leads to  
66 significant uncertainty in evaluating the evolution of BrC's light absorption capacity during atmospheric  
67 transportation. For instance, BrC emitted from biomass burning has been observed to retain strong absorption  
68 after several days of transport to the Arctic (Yue et al., 2022). In contrast, model simulations estimate BrC is  
69 nearly complete photobleaching over this timescale (Wang et al., 2018; Xu et al., 2024), which contradicts the  
70 observational evidence. Elucidating the linkage between BrC molecular composition and photobleaching rates  
71 would improve the accuracy of global-scale assessments of BrC's dynamic light absorption properties during  
72 long-range transport.

73 In this work, we performed photochemical aging experiments on three types of BrC under identical,  
74 controlled conditions, including synthesized by aqueous phase reaction (referred to "aq-BrC"), and extracted

75 from ambient (referred to “p-BrC”, where “p” denotes particulate) and biomass burning (referred to “b-BrC”)  
76 PM<sub>2.5</sub> samples. Compared to previous studies, this work systematically investigated the differences in  
77 photobleaching kinetics among various types of BrC under identical environmental conditions. We combine this  
78 with high-resolution mass spectrometry (HRMS) analysis to establish a mechanistic link between the observed  
79 divergent BrC photobleaching rates and the evolution of key molecular chromophores. In addition, we quantify  
80 the contribution of the OH oxidation pathway across all BrC types. These findings aim to provide essential  
81 parameters and a mechanistic basis for improving the representation of BrC photochemical aging in climate  
82 models.

## 83 **2. Methodology**

### 84 **2.1 Preparation of BrC**

85 Methylglyoxal (MG, 40 wt%, Merck) and ammonium sulfate (AS, 98%, Aladdin) solutions (1 mol/L) was  
86 mixed in darkness at room temperature for 2 h (pH 3.7–4.2) (Yang et al., 2024) to generate aq-BrC. Residual  
87 MG/AS were removed by solid-phase extraction (SPE) (Lin et al., 2010; Wang et al., 2017). The eluent was  
88 dried under gentle stream of ultrapure N<sub>2</sub> (>99.99%) and reconstituted in ultrapure water (18.2 MΩ·cm).  
89 Previous studies have confirmed that MG is one of the most abundant dicarbonyl species in the atmosphere (Gu  
90 et al., 2025; Fu et al., 2008), which is produced by primary emissions and oxidation of volatile organic  
91 compounds (VOCs). Considering that MG exhibit a tendency to partition into aqueous aerosols and cloud  
92 droplets in the atmosphere (Laskin et al., 2015), therefore, the secondary BrC generated by the aqueous-phase  
93 reaction between MG and AS is representative as aq-BrC.

94 PM<sub>2.5</sub> samples emitted from corn straw combustion in household stoves was collected on quartz fiber filters  
95 (25 × 20 cm, Whatman) using a high-volume sampler (TH-1000H, Wuhan Tianhong; 1.05 m<sup>3</sup>/min). Corn straw  
96 is recognized as a typical and common domestic biomass fuel in China, constituting approximately 40.0% of the  
97 total output from the agricultural products and has an estimated annual production of about 295 million tons.  
98 Therefore, PM<sub>2.5</sub> emitted from corn straw combustion was selected as typical biomass burning aerosols in this  
99 work. Figure S1 shows a schematic of sample collection process of biomass burning PM<sub>2.5</sub> samples, and Table  
100 S1 summarizes the concentrations of organic carbon (OC), element carbon (EC), the concentration of total  
101 organic carbon (TOC) of each sample. This approach closely represents real-world biomass burning emissions  
102 (Chen et al., 2019; Shan et al., 2017). For each sample, background aerosols were collected for 1 hour both  
103 before to and after the sampling period.

104 We selected five atmospheric PM<sub>2.5</sub> samples collected at Peking University Changping Campus (40°8'N,  
105 116°6'E) from 15 December 2020 to 15 January 2021 to extract p-BrC. Table S2 summarizes the sampling time  
106 and average PM<sub>2.5</sub> mass concentrations during sampling of each sample. All samples were collected using a  
107 high-volume sampler with the flow rate of 1.05 m<sup>3</sup>/min. Gaseous pollutants, PM<sub>2.5</sub> mass concentrations, non-  
108 refractory submicron particles (NR-PM<sub>1</sub>) chemical composition, and meteorology were monitored (Figure S2;  
109 details in Table S3).

110 For those PM<sub>2.5</sub> samples, twenty 1.5-cm<sup>2</sup> filter sections were ultrasonically extracted in LC-MS grade

111 methanol (Merck Inc.) for twice (20 min) to extract p-BrC and b-BrC. Extracts were dried gentle stream of  
112 ultrapure N<sub>2</sub> (>99.99%) and redissolved in ultrapure water.

## 113 2.2 Laboratory aqueous-phase photochemical aging setup

114 Photochemical aging experiments were conducted in a temperature-controlled (20 ± 0.1 °C) chamber,  
115 equipped with 20 UV bulbs (40 W;  $\lambda_{max}$  = 370 nm). The TOC of all BrC solutions were adjusted to 50 mgC/L.  
116 BrC solutions were irradiated in quartz bottles (10 mL) with added H<sub>2</sub>O<sub>2</sub> (30 wt%, Alaadin) to generate OH  
117 radicals. Steady-state OH concentrations ([OH]<sub>ss</sub>) were quantified via pseudo-first-order decay of benzoic acid  
118 (methods detailed in Text S1) (Hems and Abbatt, 2018). The average [OH]<sub>ss</sub> was (3.17 ± 0.47) × 10<sup>-14</sup> mol/L,  
119 slightly below typical cloud water maxima.

120 The transition from laboratory experimental illumination to actual solar radiation was applied by calculating  
121 the ratio between laboratory and actual spectral flux densities following the identical calculation approach used  
122 in our previous study (Qiu et al., 2024). Briefly, the scaling factor can be approximated as the ratio between the  
123 integrated spectral flux densities of two different light sources. The spectral flux densities of the UV bulbs used  
124 in this work and the 24-hour average Beijing solar spectrum at 300 m above sea level were integrated from 360  
125 nm to 380 nm (see Text S2 for detail). The 24-hour average Beijing solar spectrum was simulated using the  
126 Tropospheric Ultraviolet and Visible Radiation model (Table S4), and Figure S3 shows the comparison between  
127 calculated and measured radiation spectrum. The calculated scaling factor in this work is 3.86 (Qiu et al., 2024).  
128 Samples were collected at 0, 2, 4, 8, and 16 hours of equivalent solar radiation.

129 Furthermore, a series of control experiments were performed under H<sub>2</sub>O<sub>2</sub> free and dark conditions. In both  
130 cases, the same BrC solutions (50 mgC/L TOC) were used for different types of BrC. The former consisted of  
131 16 hours of radiation in the absence of H<sub>2</sub>O<sub>2</sub>. The dark experiments involved storing the solutions in complete  
132 darkness for an identical period (16 hours) to account for any non-photochemical changes.

133 These experiments were configured to delineate the contributions of different pathways to BrC  
134 photobleaching. The H<sub>2</sub>O<sub>2</sub> added photochemical aging experiments elucidates the synergistic effect of OH  
135 oxidation, direct BrC photolysis, and other light-independent reactions occur in dark conditions. The H<sub>2</sub>O<sub>2</sub> free  
136 experiments considered the sole contribution of the direct photolytic pathway. In addition, the dark control  
137 experiments served to investigate any potential influence of chemical reactions in dark conditions on the BrC's  
138 light-absorption capacity.

## 139 2.3 Light-absorption properties and molecular composition analysis of BrC

140 UV-Vis absorption spectra (250–700 nm) were recorded using a spectrophotometer (UV-1780, Shimadzu  
141 Inc.). MAC normalized absorption to TOC concentrations. In eq.(1),  $A_{10}^{abs}(\lambda)$ ,  $b$ , and  $c$  denotes the measured  
142 base-10 absorbance, optical path length (1 cm), and measured TOC, respectively.

$$143 \quad \text{MAC}(\lambda) = \frac{A_{10}^{abs}(\lambda) \times \ln(10)}{b \times c} \quad (1)$$

144 BrC's molecular composition was analyzed via HRMS (Orbitrap Fusion<sup>TM</sup> Tribrid<sup>TM</sup>, Thermo Scientific)

145 with electrospray ionization (ESI) in negative mode (ESI(-);  $m/z$  70–700). Samples were directly injected into  
146 HRMS at a flow rate of 10  $\mu\text{L}/\text{min}$ . Triplicate analyses ensured reproducibility, with only peaks detected in all  
147 replicates retained for assignment. Molecular formulas ( $\text{C}_x\text{H}_y\text{O}_z\text{N}_w\text{S}_n$ ;  $x = 1\text{--}90$ ,  $y = 1\text{--}200$ ,  $z = 0\text{--}20$ ,  $w = 0\text{--}3$ ,  
148  $n = 0\text{--}1$ ) were assigned with  $m/z$  error lower than  $\pm 0.005$  Da. The H/C, O/C, N/C, and S/C atom ratios for each  
149 assigned formula were constrained to 0.3–3.0, 0–3.0, 0–0.5, and 0–2.0, respectively (Wang et al., 2017). Signal-  
150 intensity-weighted average elemental compositions (eq.(2)), O/C atom ratios, and N/C atom ratios (eq.(3)) were  
151 calculated as:

$$152 \quad Y = \frac{\sum_i x_i Y_i}{\sum_i x_i}, \text{ where } Y = \text{C, H, O, N, and S} \quad (2)$$

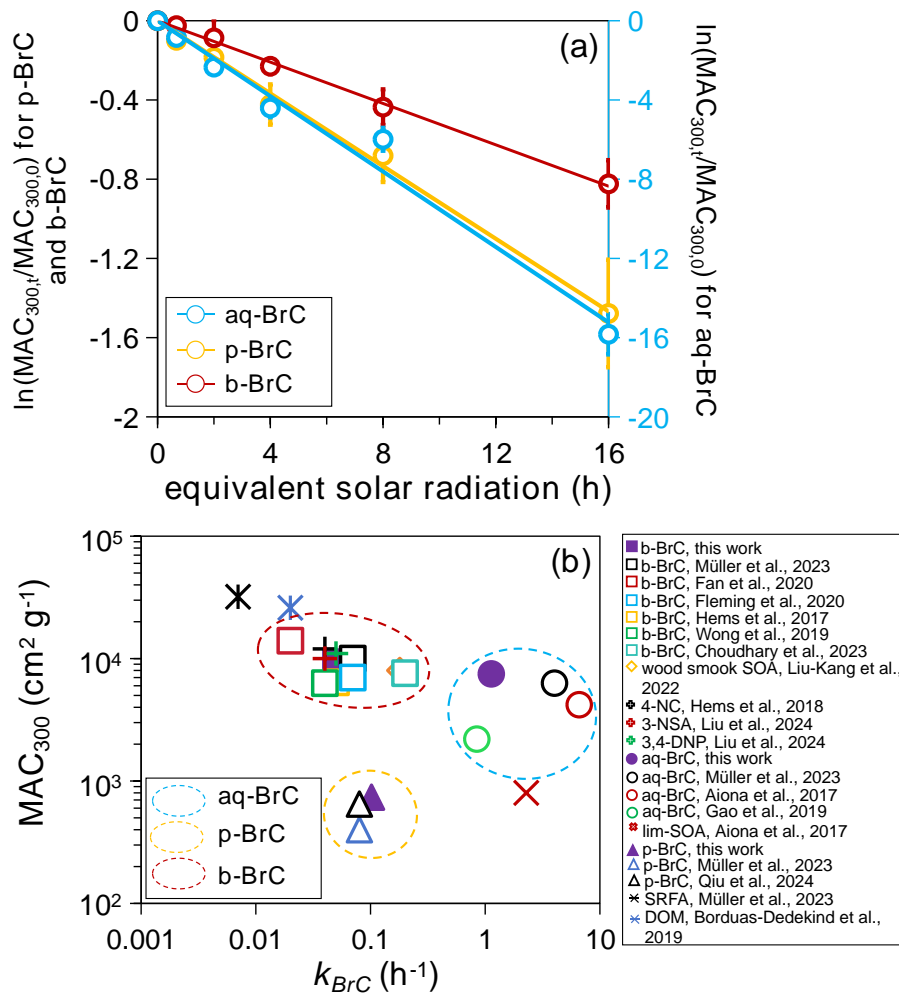
$$153 \quad Y/Z = \frac{\sum_i x_i Y_i}{\sum_i x_i Z_i}, \text{ where } Y/Z = \text{O/C or N/C} \quad (3)$$

154 where  $x_i$  in eqs. (2) and (3) indicated the signal-intensity-weighted factor.

### 155 **3. Results and Discussion**

#### 156 **3.1 Quantification and Comparison of BrC Photobleaching Rates**

157 Given that BrC's light-absorption properties at shorter wavelengths are a better indicator of its  
158 photobleaching kinetics (Aiona et al., 2017), we focused our analysis on the variation in the MAC at 300 nm  
159 ( $\text{MAC}_{300}$ ). The measured  $\text{MAC}_{300}$  of aq-BrC, p-BrC, and b-BrC is  $(7.32 \pm 0.89) \times 10^3 \text{ cm}^2 \text{ g}^{-1}$ ,  $(7.38 \pm 0.83) \times$   
160  $10^2 \text{ cm}^2 \text{ g}^{-1}$ , and  $(9.44 \pm 0.71) \times 10^3 \text{ cm}^2 \text{ g}^{-1}$ , respectively. Figure 1(a) shows the overall decay of  $\text{MAC}_{300}$  for  
161 different BrC types, plotted as the natural logarithm of the ratio ( $\ln(\text{MAC}_{300,t}/\text{MAC}_{300,0})$ ) versus irradiation hours.  
162 The left axis of Figure 1(a) shows the variation in  $\ln(\text{MAC}_{300,t}/\text{MAC}_{300,0})$  for p-BrC and b-BrC, while the right  
163 axis denotes this variation for aq-BrC. Here,  $\text{MAC}_{300,t}$  and  $\text{MAC}_{300,0}$  denote the  $\text{MAC}_{300}$  after  $t$  hours of  
164 irradiation and its initial value, respectively. The observed linear decay demonstrates that BrC undergoes  
165 photobleaching regardless of its source. The aq-BrC has been almost completely bleached in the initial 2 hours.  
166 The  $\text{MAC}_{300}$  decreased by 77.2% after 16 hours of radiation. In comparison, for b-BrC, the  $\text{MAC}_{300}$  only  
167 decreased by 56.1%. Even after extending to 32 hours of radiation, b-BrC still kept strong light-absorption  
168 capacity (see Figure S4). The differences in the variation in  $\text{MAC}_{300}$  for different types of BrC demonstrate that  
169 aq-BrC undergoes rapid photobleaching in the presence of solar radiation, while b-BrC exhibits stable light-  
170 absorption capacity during photobleaching.



171  
 172 **Figure 1** (a) Variations in the  $\ln(\text{MAC}_{300,t}/\text{MAC}_{300,0})$  of aq-BrC (blue plots, right axis), p-BrC (yellow plots, left  
 173 axis), and b-BrC (red plots, left axis) as a function of radiation hours. Blue, yellow, and red lines indicate fitted  
 174  $k_{BrC}$  of aq-BrC, p-BrC, and b-BrC. Error bars represent one standard deviation of datapoints derive from three  
 175 (aq-BrC and b-BrC) or five (p-BrC) parallel experiments. (b) The relationship between  $\text{MAC}_{300}$  and calculated  
 176  $k_{BrC}$  of different types of BrC in this work and other studies. 4-NC, 3-NSA, 3,4-DNP, SRFA, and DOM represents  
 177 4-nitrocateol, 3-mitrosalicylic acid, 3,4-dinitrophenol, Suwannee River fulvic acid standard, and dissolved  
 178 organic matters, respectively. Blue, yellow, and red circles marked aq-BrC (including BrC generated via  
 179 aldehyde-amine condensation reactions), p-BrC, and b-BrC (including representative compounds emitted from  
 180 biomass burning). The exact  $\text{MAC}_{300}$  values are obtained from figures in corresponding literatures, and  $k_{BrC}$  are  
 181 calculated based on the  $\text{MAC}_{300}$  and hours of radiation.

182 The liner decline in  $\ln(\text{MAC}_{300,t}/\text{MAC}_{300,0})$  indicates that BrC photobleaching fitted the pseudo-first order  
 183 kinetic, which was represented by the negative slope of  $\ln(\text{MAC}_{300,t}/\text{MAC}_{300,0})$  vs. radiation hours:

184 
$$\text{MAC}_{300,t} = \text{MAC}_{300,0} \times \exp(-k_{BrC}t) \quad (4)$$

185 where  $k_{BrC}$  is the overall photobleaching rate constant. The calculated  $k_{BrC}$  of aq-BrC, p-BrC, and b-BrC were  
 186  $(1.13 \pm 0.08) \text{ hour}^{-1}$ ,  $(0.12 \pm 0.02) \text{ hour}^{-1}$ , and  $(0.05 \pm 0.01) \text{ hour}^{-1}$ , respectively. Correspondingly, the lifetime of

187 BrC ( $\tau_{BrC}$ , indicated by BrC's absorption decreased to 1/e of its initial value) (Schnitzler et al., 2022) were 1.05  
188 hours, 10.91 hours, and 19.16 hours, respectively. Longer  $\tau_{BrC}$  of b-BrC indicates its absorption largely retains  
189 during atmospheric transportation process. This order-of-magnitude difference in  $k_{BrC}$  among three BrC types,  
190 quantified under comparable conditions, highlights a fundamental source dependency that cannot be attributed  
191 to environmental condition variability. This clear difference necessitates a molecular-level explanation, which  
192 we pursue by examining the dominant bleaching pathway and the underlying chemical composition.

193 Figure 1(b) presents a comparison of  $MAC_{300}$  versus overall  $k_{BrC}$  for BrC from various sources, including  
194 data from this study and other studies (data and references in Table S5). Based on their sources, we classified  
195 aq-BrC (including BrC generated via aldehyde-amine condensation reactions), p-BrC, and b-BrC (including  
196 representative compounds emitted from biomass burning) in three different clusters. Our results are comparable  
197 to those of previous studies. The characteristic of aq-BrC is strong absorption, rapid photobleaching. This  
198 demonstrates that the light-absorption capacity of BrC generated by secondary atmospheric aqueous phase  
199 reactions (De Haan et al., 2017) decrease rapidly in the presence of solar radiation. In stark contrast, b-BrC  
200 shows strong absorption but slow photobleaching, implying its stable strong absorption in the atmosphere. p-  
201 BrC exhibits weak absorption and slow photobleaching, which has also been observed in different urban areas,  
202 including Eastern China (Qiu et al., 2024), India (Dasari et al., 2019), Northern Europe (Müller et al., 2023), and  
203 the United States (Chen et al., 2021). It is noteworthy that p-BrC contains a mixture of primary and secondary  
204 BrC that is challenging to separate quantitatively. However, from molecular composition and solar radiation  
205 during sampling, p-BrC is considered to be predominantly of primary emissions. Herein, we further analyzed  
206 the molecular composition of p-BrC following the non-target analysis approach used in our previous study (Qiu  
207 et al., 2024), more details were described in Text S3. Figure S5 shows the molecular composition and relevant  
208 solar radiation during sampling, which is represented by the 75<sup>th</sup> percentile solar radiation ( $Rad_{75}$ ). Low  $Rad_{75}$   
209 showed limited photochemical aging prior to analysis, and high mass fraction of nitrophenols proved the  
210 dominate role of primary emission for p-BrC.

211 Having investigated the differences in overall photobleaching rates across different BrC types, we further  
212 elucidated the underlying mechanisms by assessing the contribution of each photobleaching pathway. Previous  
213 studies suggest that BrC photobleaching occurs via three different pathways, including direct photolysis, OH  
214 oxidation, and other light-independent reactions occur in dark conditions (Gao and Zhang, 2019; Liu-Kang et  
215 al., 2022; Wong et al., 2019). Choudhary et al. (2023) (Choudhary et al., 2023) have demonstrated that in the  
216 presence of  $H_2O_2$ , the overall  $k_{BrC}$  can be expressed as a linear sum of the pseudo first-order effective  
217 photobleaching rate constant due to OH oxidation ( $k_{BrC,OH}$ ), BrC direct photolysis ( $k_{BrC,pho}$ ), and other light-  
218 independent reactions occur in dark conditions ( $k_{BrC,ctrl}$ ), see eq. (5):

$$219 \quad k_{BrC} = k_{BrC,OH} + k_{BrC,pho} + k_{BrC,ctrl} \quad (5)$$

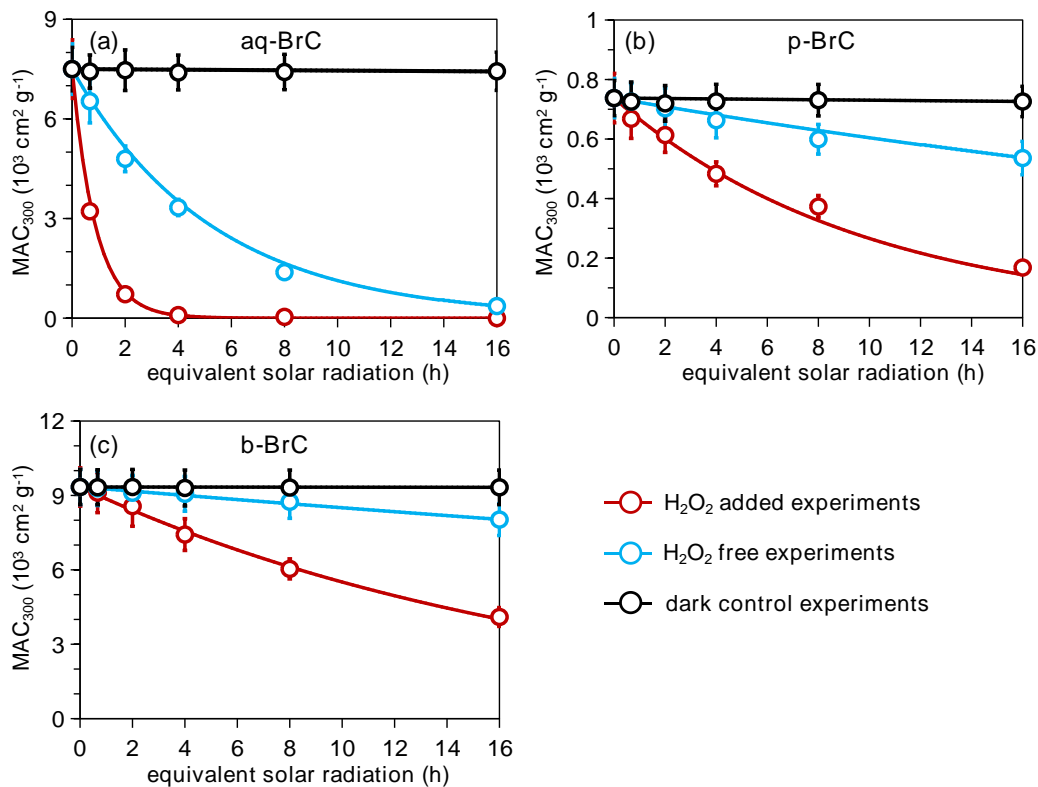
220 The  $k_{BrC,pho}$  and  $k_{BrC,ctrl}$  are derived from the pseudo-first-order decay of  $MAC_{300}$  in  $H_2O_2$  free experiments  
221 and dark control experiments, respectively, using the calculation approach identical to eq. (4) and the  
222 experimental procedures detailed in Section 2.2. Therefore, although  $k_{BrC,OH}$  cannot be measured directly, it can  
223 be indirectly determined by calculating the difference between the overall  $k_{BrC}$  and the sum of  $k_{BrC,pho}$  (from  $H_2O_2$   
224 free experiments) and  $k_{BrC,ctrl}$  (from dark control experiments).

**Table 1** The  $k_{BrC,ctrl}$ ,  $k_{BrC,pho}$ , and  $k_{BrC,OH}$  for different BrC types

BrC type	$k_{BrC,ctrl}$	$k_{BrC,pho}$	$k_{BrC,OH}$
aq-BrC	$(0.004 \pm 0.002) \text{ h}^{-1}$	$(0.19 \pm 0.03) \text{ h}^{-1}$	$(0.94 \pm 0.06) \text{ h}^{-1}$
p-BrC	$(0.007 \pm 0.001) \text{ h}^{-1}$	$(0.02 \pm 0.005) \text{ h}^{-1}$	$(0.08 \pm 0.02) \text{ h}^{-1}$
b-BrC	$(0.006 \pm 0.002) \text{ h}^{-1}$	$(0.01 \pm 0.004) \text{ h}^{-1}$	$(0.04 \pm 0.01) \text{ h}^{-1}$

226 Figure 2 displays the variations in  $MAC_{300}$  in photochemical aging experiments (with  $H_2O_2$ , red line,  
 227 representing the synergistic effect of OH oxidation, direct BrC photolysis, and other light-independent reactions  
 228 occur in dark conditions),  $H_2O_2$  free experiments (blue line, representing the contribution of BrC direct  
 229 photolysis), and dark control experiments (black line, representing the contribution of other light-independent  
 230 reactions occur in dark conditions). It is noted that for dark control experiments, the x-axis denotes the time the  
 231 BrC solution is kept under dark conditions. Table 1 summarizes the  $k_{BrC,ctrl}$ ,  $k_{BrC,pho}$ , and  $k_{BrC,OH}$  for different BrC  
 232 types. Specifically,  $MAC_{300}$  variations were negligible in dark controls, rendering the calculated  $k_{BrC,ctrl}$  was close  
 233 to 0. For all BrC types,  $k_{BrC,pho}$  was substantially lower than  $k_{BrC,OH}$ . The overwhelming contribution of  $k_{BrC,OH}$   
 234 (over 80% of  $k_{BrC}$ ) unambiguously identifies OH oxidation as the dominant mechanism governing BrC  
 235 photobleaching. The dominate role of OH oxidation in BrC photobleaching have been also proved in several  
 236 previous studies (Choudhary et al., 2023; Hems and Abbatt, 2018; Zhao et al., 2015), this work provide  
 237 quantitative and comparative evidence regardless of BrC types. Consequently, the observed differences in  $k_{BrC}$   
 238 among different types of BrC can be fundamentally attributed to the molecular-composition-dependent reactivity  
 239 of BrC components toward OH radicals. Hence, understanding the underlying molecular composition that  
 240 determine a BrC molecule's susceptibility to this OH oxidation.

241 It is important to note that the laboratory-synthesized aq-BrC represents a simplified chemical system.  
 242 While it provides a clear mechanistic understanding of rapid photobleaching driven by BrC chromophores with  
 243 high chemical reactivity, real atmospheric aqueous-phase processes involve more complex precursors and  
 244 mixtures, yielding secondary BrC with different photobleaching kinetics. Nevertheless, the dominate role of OH  
 245 oxidation established in this work, which provides a critical lens through which to interpret the slower  
 246 photobleaching rates of the more complex ambient (p-BrC) and biomass burning (b-BrC) samples.



247  
 248 **Figure 2** The variations in MAC<sub>300</sub> in photochemical aging experiments (with H<sub>2</sub>O<sub>2</sub>, red line, representing the  
 249 synergistic effect of OH oxidation, direct BrC photolysis, and other light-independent reactions occur in dark  
 250 conditions), H<sub>2</sub>O<sub>2</sub> free experiments (blue line, representing the variation in MAC<sub>300</sub> contributed by BrC direct  
 251 photolysis), and dark control experiments (black line, representing the variation in MAC<sub>300</sub> contributed by other  
 252 light-independent reactions occur in dark conditions) for (a) aq-BrC, (b) p-BrC, and (c) b-BrC, respectively. For  
 253 dark control experiments (black line), the x-axis represents the time the BrC solution is kept in the absence of  
 254 light.

### 255 3.2 Chemical investigation of different BrC photobleaching rates

256 To elucidating the differences in BrC photobleaching rates, we investigated BrC's molecular composition  
 257 before and after photobleaching, which was represented by BrC's molecular composition after 16 hours of  
 258 radiation.

259 Table 2 summarizes the signal-intensity-weighted average elemental compositions, molecular weights, O/C  
 260 ratios, and N/C ratios of different types of BrC before and after 16 hours of radiation. The observed decrease in  
 261 average molecular weights upon photobleaching across all BrC types, alongside an elevated O/C ratio, points to  
 262 the production of more oxidized, lower-mass species. Additionally, we found the mass concentrations of low-  
 263 molecular-weight organic acids (formic acid, acetic acid, and oxalic acid; see Figure S6) significantly increased  
 264 with longer radiation hours, demonstrating carbon backbone fragmentation (Borduas-Dedekind et al., 2019).  
 265 Figure S7 demonstrates that more products with lower C atom numbers are detected after photobleaching, further  
 266 proves the carbon backbone fragmentation. Considering OH oxidation dominates BrC photobleaching, the

267 molecular-level evolution aligns with OH-mediated degradation pathways (Hems et al., 2020; Qiu et al., 2024;  
 268 Liu et al., 2025): (i) electrophilic addition to unsaturated bonds (like C=C bonds) and (ii) subsequent carbon  
 269 backbone fragmentation.

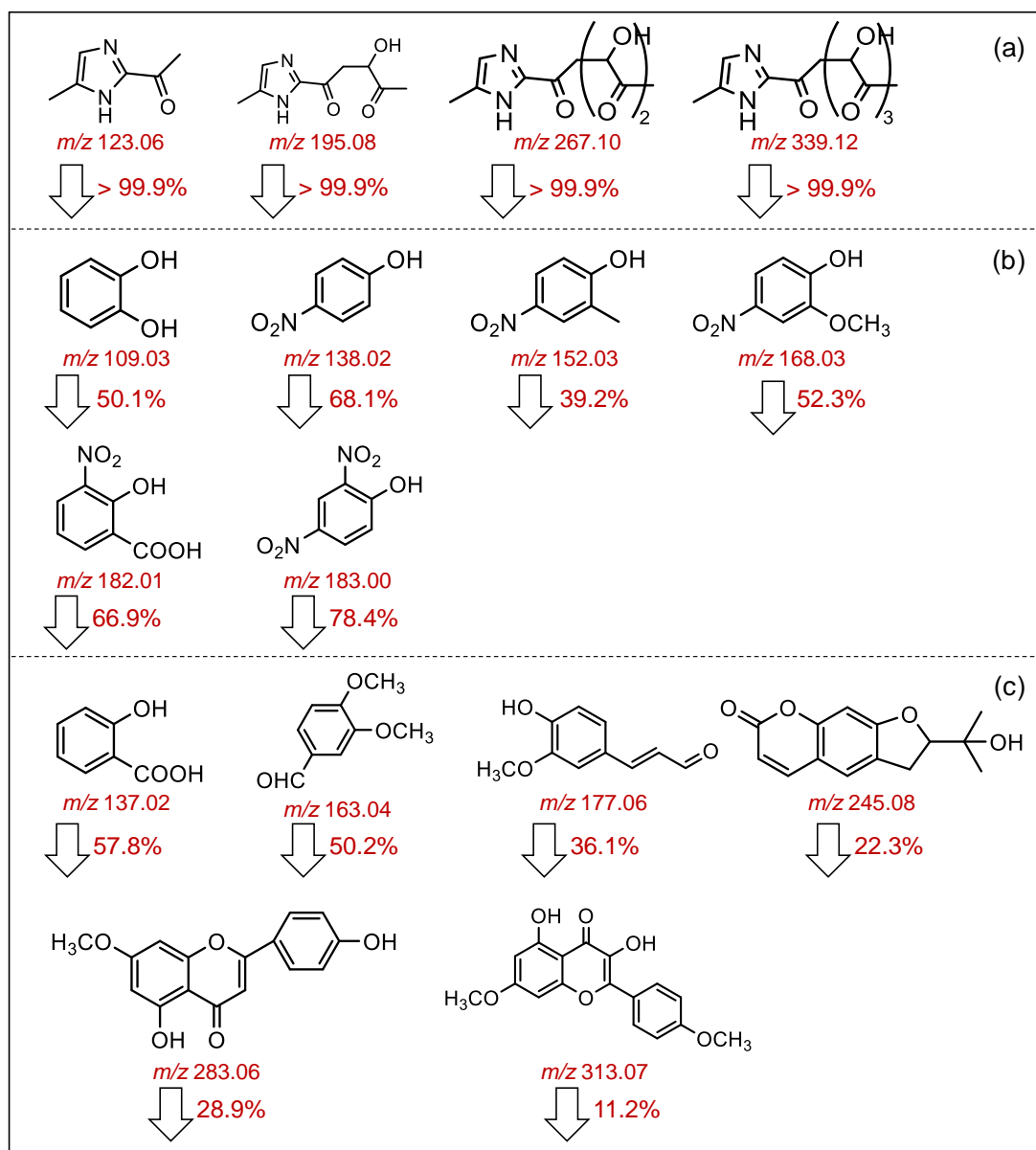
270 In addition, the reduced N/C atom ratios (Table 2) further confirmed degradation of N-containing  
 271 compounds, which are key UV-Vis absorbers contributing significantly to BrC absorption (Lin et al., 2017; Wang  
 272 et al., 2019; Zeng et al., 2021; Li et al., 2025). The formation of compounds with higher oxidation states and the  
 273 degradation of N-containing compounds reduce the conjugation degrees of BrC, diminishing  $\pi \rightarrow \pi^*$  electronic  
 274 transitions and weakening light-absorption capacity.

275 **Table 2** Variations in the signal-intensity-weighted average elemental compositions, molecular weights,  
 276 O/C ratios, and N/C ratios of different types of BrC before and after photobleaching

aq-BrC	elemental composition	molecular weight	O/C	N/C
before	C <sub>8.94</sub> H <sub>10.22</sub> O <sub>4.64</sub> N <sub>1.33</sub>	210.36	0.52	0.15
after	C <sub>8.22</sub> H <sub>10.17</sub> O <sub>4.66</sub> N <sub>1.07</sub>	198.35	0.57	0.12
p-BrC	elemental composition	molecular weight	O/C	N/C
before	C <sub>7.88</sub> H <sub>8.38</sub> O <sub>2.47</sub> N <sub>2.13</sub> S <sub>0.65</sub>	193.08	0.31	0.28
after	C <sub>7.21</sub> H <sub>9.17</sub> O <sub>2.52</sub> N <sub>1.82</sub> S <sub>0.68</sub>	183.25	0.35	0.25
b-BrC	elemental composition	molecular weight	O/C	N/C
before	C <sub>15.92</sub> H <sub>16.68</sub> O <sub>6.05</sub> N <sub>1.18</sub> S <sub>0.31</sub>	330.96	0.38	0.08
after	C <sub>15.42</sub> H <sub>16.92</sub> O <sub>6.11</sub> N <sub>1.07</sub> S <sub>0.41</sub>	327.82	0.40	0.07

277 Subsequently, we determined representative BrC chromophores relate to the photobleaching of different  
 278 types of BrC based on the following three criteria. Firstly, we calculated the differential HRMS spectra of  
 279 different types of BrC before and after photobleaching (Figure S8). These peaks with negative intensities (> 3  
 280 times the signal-to-noise ratio) denote species consumed after photobleaching. Secondly, these candidate species  
 281 were cross-compared to identify compounds that were highly characteristic of each specific source. Lastly,  
 282 tandem HRMS (HRMS<sup>2</sup>) analysis was adopted to determine the chemical structure of selected BrC  
 283 chromophores.

284 In this work, the photooxidation of MG and imidazole-2-carboxaldehyde (2-IC) oligomers (Aiona et al.,  
 285 2017) with formula C<sub>3n</sub>H<sub>4n</sub>N<sub>2</sub>O<sub>2n-3</sub> (n = 2-5; including *m/z* 123.06, 195.08, 267.10, and 339.12), phenols and  
 286 nitrophenols (Hems and Abbatt, 2018; Magalhães et al., 2017) (including *m/z* 109.03, 138.02, 152.03, 168.03,  
 287 182.01, and 183.00), and lignin derivatives (Fleming et al., 2020) (including *m/z* 137.02, 163.04, 245.08, 283.06,  
 288 and 313.07) were identified as the dominant reactions in the photobleaching of aq-BrC, p-BrC, and b-BrC,  
 289 respectively. Compounds identified as products after photobleaching for aq-BrC, p-BrC, and b-BrC are  
 290 respectively summarized in Tables S6-S8. It is acknowledged that secondary BrC comprises a wide variety of  
 291 compounds formed through different pathways. While phenols and nitrophenols identified here can themselves  
 292 be secondary products, their markedly slower photobleaching rate (compared to the MG/AS-derived aq-BrC in  
 293 this work) highlights the substantial kinetic diversity within the broader secondary BrC. This further reinforces  
 294 that the molecular architecture, rather than the primary or secondary classification, is the fundamental  
 295 determinant of BrC photochemical stability.



296

297 **Figure 3** The chemical structures of (a) MG and 2-IC oligomers detected in aq-BrC; (b) phenols and nitrophenols  
 298 detected in p-BrC, and (c) lignin derivatives detected in b-BrC. The detected  $m/z$  for these compounds are marked  
 299 under their structures. The ratios of decline in signal intensities for these compounds after 16 hours of radiation  
 300 are indicated next to the bottom arrows.

301 Figure 3 displays the chemical structures of these MG and 2-IC oligomers, phenols and nitrophenols, and  
 302 lignin derivatives, as well as the declines in their signal intensities after 16 hours of radiation. Variations in  
 303 HRMS signal intensities represent the changes in the mass concentrations, though specific mass concentrations  
 304 cannot be derived. Figure 3(a) illustrates the predominant molecular species and the corresponding decline in  
 305 MG and 2-IC oligomers during the photobleaching of aq-BrC. Following photobleaching, these oligomers  
 306 became undetectable (signal-to-noise ratio < 3), experiencing a reduction in signal intensity of >99.9% (Figure

307 3(a)). This observation is consistent with the nearly complete bleaching of aq-BrC. The high reactivity of the  
308 chain structures of MG and 2-IC oligomers with OH radicals (Aiona et al., 2017) explains the elevated  $k_{BrC}$  value  
309 observed for aq-BrC.

310 As shown in Figure 3(b), a greater number of electron-withdrawing substituents on the benzene ring  
311 correlates with a more significant decline of signal intensity after photobleaching. For instance, 2-methyl-4-  
312 nitrophenol ( $m/z$  152.03), which bears an electron-donating methyl group in addition to the electron-withdrawing  
313 nitro substituent present in 4-nitrophenol ( $m/z$  138.02), demonstrates a comparatively lower signal attenuation  
314 of 39.2% after photobleaching, whereas 4-nitrophenol exhibits a signal decrease of 68.1%. The electron-  
315 withdrawing substituents exert both inductive and resonance effects, effectively diminishing the electron density  
316 of the  $\pi$ -system of the aromatic ring. This electron-deficient state enhances the susceptibility of these species to  
317 nucleophilic attack by OH radicals, thereby facilitating their photooxidation and contributing to the observed  
318 photobleaching behavior. However, the reactivity of these species remains lower than that of MG and 2-IC  
319 oligomers, which explains lower  $k_{BrC}$  for p-BrC compares to aq-BrC.

320 In comparison, the signal intensities of the majority of lignin derivatives only decreased by below 50%,  
321 corresponding to the lowest  $k_{BrC}$  for b-BrC (Figure 3(c)). Specifically, nodakenetin and flavonoids ( $m/z$  245.08,  
322 283.06, and 313.07) exhibit highly stabilized molecular structures, wherein the aromatic rings conjugated with  
323 oxygen-containing heterocyclic moieties significantly reduce their chemical reactivity, resulting in low  $k_{BrC}$  for  
324 b-BrC. The chemical stability of lignin derivatives has been also proved by previous laboratory experiment  
325 (Wong et al., 2019). However, studies found that levoglucosan, which is an important component in biomass  
326 burning aerosols, may be oxidized by OH radicals and therefore slow down the reaction of other BrC  
327 chromophores reacting with OH (Bai et al., 2013; Zhao et al., 2014). In this work, the same TOC mass  
328 concentrations (50 mg/L) across all BrC types provides equal total potential OH sinks, making the observed  
329 order-of-magnitude difference in  $k_{BrC}$  more likely attributable to the reactivity of the chromophores themselves  
330 rather than solely to differences in competitor abundance. Additionally, the identified lignin derivatives exhibited  
331 low signal decay percentages despite being exposed to the same  $[OH]_{ss}$  as the highly reactive BrC chromophores.  
332 Hence, it is expected that the chemical stability of lignin derivative leads to the low  $k_{BrC}$  for b-BrC.

333 We noted that the exact variation in the mass concentration of compounds shown in Figure 3 were not  
334 derived in this work. Ultra-high performance liquid chromatography (UHPLC)-HRMS analysis using standards  
335 or surrogate standards should be adopted to obtain the mass concentration of these compounds. However, this  
336 work aims to comparatively track the changes in molecular composition for each specific BrC type before and  
337 after photobleaching. While absolute quantification is not feasible based on HRMS analysis, the relative changes  
338 in signal intensity for a given compound are comparable within the same sample matrix. Therefore, the variation  
339 in signal intensity for a specific  $m/z$  can be reliably interpreted as a corresponding change in its relative mass  
340 concentration.

341 In addition, while the species highlighted in Figure 3 were rigorously selected as representative and reactive  
342 chromophores through the differential screening and structural identification process described above, we fully  
343 acknowledge that our analysis may not capture all potential BrC chromophores. Limitations in analytical  
344 sensitivity, chromatographic separation, and the chemical complexity of BrC result in several BrC chromophores,

345 particularly those at low concentrations or with poor ionization efficiency, might not be detected or their changes  
346 fully characterized. Therefore, while the reported decay percentages for the identified species are robust, the  
347 total BrC photobleaching likely involves contributions from additional chromophores not specifically tracked  
348 here.

#### 349 **4. Conclusion and Atmospheric Implication**

350 This work quantifies the  $k_{BrC}$  for three different types of BrC and demonstrates that their order-of-magnitude  
351 differences (aq-BrC > p-BrC > b-BrC) originate from distinct molecular susceptibilities to OH-driven oxidation  
352 through controlled comparative experiments. While the source dependency of BrC photobleaching has been  
353 suggested, our study mechanistically establishes the linkage between BrC photobleaching kinetics and molecular  
354 composition. Specifically, rapid photobleaching of aq-BrC is governed by the high OH reactivity of MG and 2-  
355 IC oligomers; in comparison, the remarkable stability of b-BrC is attributed to resilient, conjugated aromatic  
356 systems in lignin derivatives. For p-BrC, an intermediate  $k_{BrC}$  was observed, consistent with the oxidation  
357 kinetics of nitrophenolic chromophores. Critically, we show that OH oxidation accounts for >80% of the total  
358 photobleaching across all sources, identifying it as the dominant and unifying chemical pathway under aqueous  
359 conditions.

360 These quantified, source-dependent  $k_{BrC}$  values and their molecular-level changes emphasizes the  
361 necessitate explicit consideration of source variability when evaluating BrC's radiative effect. Current models  
362 often assume constant  $k_{BrC}$  based on simplified representative compounds or field data (Hems and Abbatt, 2018;  
363 Schnitzler et al., 2022; Wang et al., 2018), yet substantial discrepancies exist. For instance, the reported  $k_{BrC}$   
364 values differ by approximately an order of magnitude between field observations and laboratory simulations  
365 (Schnitzler et al., 2022; Wang et al., 2018). Spatiotemporal heterogeneity in BrC sources (Xiong et al., 2022)  
366 (fossil fuel/biomass combustion, secondary formation) drives global regional variations in  $k_{BrC}$ . We should  
367 acknowledge that though source-dependent BrC photobleaching rates are essential in assessing BrC's global  
368 DRE, the impact of environmental conditions like temperature and relative humidity are also decisive (Schnitzler  
369 et al., 2022).

370 In addition, the low  $k_{BrC}$  for b-BrC explains unexpectedly high BrC absorption in remote regions (e.g., the  
371 Arctic). Field data confirm biomass burning contributes 57% of Arctic BrC while < 10% for secondary BrC (Yue  
372 et al., 2022). Previous studies have confirmed that biomass burning aerosols contains substantial amounts of  
373 lignin derivatives (Wong et al., 2019), which exhibit strong light-absorbing properties and chemical stability in  
374 OH oxidation. Therefore, during the long-range transport (Zhang et al., 2025), b-BrC is expected to retain strong  
375 absorption, leading to enhancement of the aerosol DRE over large spatial scales. On a global scale, one major  
376 source of b-BrC is wildfire events (Wang et al., 2025; Shen et al., 2024; Bond et al., 2004). With the increasing  
377 frequency of wildfires (Yue et al., 2013; Hurteau et al., 2014; Cunningham et al., 2024; Jain et al., 2022), the  
378 emission of b-BrC is expected to rise correspondingly. In all, b-BrC would exert a significant influence on BrC's  
379 global radiative effect.

380 **Associate Content**

381 **Code and Data Availability**

382 The data used in this study is available upon request from the corresponding author (zhijunwu@pku.edu.cn).

383 **Author Contributions**

384 Y.Q. and Z.W. designed this work. Y.Q., T.Q., Y.G., and D.L. collected and analyzed the measurement data.  
385 Y.Q., T.Q., Y.L., and R.M. analyzed UHPLC-MS data. Z.W. and M.H. edited the manuscript. All authors have  
386 read and agreed to submit this manuscript.

387 **Funding**

388 This work is funded by National Natural Science Foundation of China – Youth Program (42507137), China  
389 Postdoctoral Science Foundation (2025M771267), and the National Key Research and Development Program  
390 of China (2022YFC3701000, Task 4).

391 **Competing Interests**

392 The authors declare that they have no conflict of interest.

393 **Acknowledgements**

394 This research has been supported by the National Natural Science Foundation of China (grant no.  
395 42507137), Chinese Postdoctoral Science Foundation (grant no. 2025M771267), the National Key Research and  
396 Development Program of China (grant no. 2022YFC3701000, Task 4).

397

## 398 **References**

- 399 Aiona, P. K., Lee, H. J., Leslie, R., Lin, P., Laskin, A., Laskin, J., Nizkorodov, S. A.: Photochemistry of Products  
400 of the Aqueous Reaction of Methylglyoxal with Ammonium Sulfate. *ACS Earth and Space Chemistry*. 1, 522-532.  
401 <https://doi.org/10.1021/acsearthspacechem.7b00075>, 2017.
- 402 Bai, J., Sun, X., Zhang, C., Xu, Y., Qi, C.: The OH-initiated atmospheric reaction mechanism and kinetics for  
403 levoglucosan emitted in biomass burning. *Chemosphere*. 93, 2004-2010.  
404 <https://doi.org/10.1016/j.chemosphere.2013.07.021>, 2013.
- 405 Bond, T. C.: Spectral dependence of visible light absorption by carbonaceous particles emitted from coal  
406 combustion. *Geophysical Research Letters*. 28, 4075-4078. <https://doi.org/10.1029/2001GL013652>, 2001.
- 407 Bond, T. C., Streets, D. G., Yarber, K. F., Nelson, S. M., Woo, J.-H., Klimont, Z.: A technology-based global  
408 inventory of black and organic carbon emissions from combustion. *Journal of Geophysical Research: Atmospheres*.  
409 109. <https://doi.org/10.1029/2003JD003697>, 2004.
- 410 Borduas-Dedekind, N., Ossola, R., David, R. O., Boynton, L. S., Weichlinger, V., Kanji, Z. A., McNeill, K.:  
411 Photomineralization mechanism changes the ability of dissolved organic matter to activate cloud droplets and to  
412 nucleate ice crystals. *Atmospheric Chemistry and Physics*. 19, 12397-12412. [https://doi.org/10.5194/acp-19-12397-](https://doi.org/10.5194/acp-19-12397-2019)  
413 [2019](https://doi.org/10.5194/acp-19-12397-2019), 2019.
- 414 Brown, H., Liu, X., Pokhrel, R., Murphy, S., Lu, Z., Saleh, R., Mielonen, T., Kokkola, H., Bergman, T., Myhre,  
415 G., Skeie, R. B., Watson-Paris, D., Stier, P., Johnson, B., Bellouin, N., Schulz, M., Vakkari, V., Beukes, J. P., van Zyl,  
416 P. G., Liu, S., Chand, D.: Biomass burning aerosols in most climate models are too absorbing. *Nature Communications*.  
417 12, 277. <https://doi.org/10.1038/s41467-020-20482-9>, 2021.
- 418 Chen, L.-W. A., Chow, J. C., Wang, X., Cao, J., Mao, J., Watson, J. G.: Brownness of Organic Aerosol over the  
419 United States: Evidence for Seasonal Biomass Burning and Photobleaching Effects. *Environmental Science &*  
420 *Technology*. 55, 8561-8572. <https://doi.org/10.1021/acs.est.0c08706>, 2021.
- 421 Chen, Q., Sun, H., Wang, J., Shan, M., Yang, X., Deng, M., Wang, Y., Zhang, L.: Long-life type — The dominant  
422 fraction of EPFRs in combustion sources and ambient fine particles in Xi'an. *Atmos. Environ*. 219, 117059.  
423 <https://doi.org/10.1016/j.atmosenv.2019.117059>, 2019.
- 424 Choudhary, V., Roson, M. L., Guo, X., Gautam, T., Gupta, T., Zhao, R.: Aqueous-phase photochemical oxidation  
425 of water-soluble brown carbon aerosols arising from solid biomass fuel burning. *Environmental Science: Atmospheres*.  
426 3, 816-829. <https://doi.org/10.1039/D2EA00151A>, 2023.
- 427 Chung, C. E., Ramanathan, V., Decremier, D.: Observationally constrained estimates of carbonaceous aerosol  
428 radiative forcing. *Proceedings of the National Academy of Sciences USA*. 109, 11624-11629.  
429 <https://doi.org/10.1073/pnas.1203707109>, 2012.
- 430 Corr, C. A., Hall, S. R., Ullmann, K., Anderson, B. E., Beyersdorf, A. J., Thornhill, K. L., Cubison, M. J., Jimenez,  
431 J. L., Wisthaler, A., Dibb, J. E.: Spectral absorption of biomass burning aerosol determined from retrieved single

432 scattering albedo during ARCTAS. *Atmospheric Chemistry and Physics*. 12, 10505-10518.  
433 <https://doi.org/10.5194/acp-12-10505-2012>, 2012.

434 Cunningham, C. X., Williamson, G. J., Bowman, D. M. J. S.: Increasing frequency and intensity of the most  
435 extreme wildfires on Earth. *Nature Ecology & Evolution*. 8, 1420-1425. <https://doi.org/10.1038/s41559-024-02452-2>,  
436 2024.

437 Dalton, A. B., Nizkorodov, S. A.: Photochemical Degradation of 4-Nitrocatechol and 2,4-Dinitrophenol in a  
438 Sugar-Glass Secondary Organic Aerosol Surrogate. *Environmental Science & Technology*. 55, 14586-14594.  
439 <https://doi.org/10.1021/acs.est.1c04975>, 2021.

440 Dasari, S., Andersson, A., Bikkina, S., Holmstrand, H., Budhavant, K., Satheesh, S., Asmi, E., Kesti, J., Backman,  
441 J., Salam, A., Bisht, D. S., Tiwari, S., Hameed, Z., Gustafsson, Ö.: Photochemical degradation affects the light  
442 absorption of water-soluble brown carbon in the South Asian outflow. *Science Advances*. 5, eaau8066.  
443 <https://doi.org/10.1126/sciadv.aau8066>, 2019.

444 De Haan, D. O., Hawkins, L. N., Welsh, H. G., Pednekar, R., Casar, J. R., Pennington, E. A., de Loera, A., Jimenez,  
445 N. G., Symons, M. A., Zauscher, M., Pajunoja, A., Caponi, L., Cazaunau, M., Formenti, P., Gratien, A., Pangu, E.,  
446 Doussin, J.-F.: Brown Carbon Production in Ammonium- or Amine-Containing Aerosol Particles by Reactive Uptake  
447 of Methylglyoxal and Photolytic Cloud Cycling. *Environmental Science & Technology*. 51, 7458-7466.  
448 <https://doi.org/10.1021/acs.est.7b00159>, 2017.

449 Fan, X., Yu, X., Wang, Y., Xiao, X., Li, F., Xie, Y., Wei, S., Song, J., Peng, P. a.: The aging behaviors of  
450 chromophoric biomass burning brown carbon during dark aqueous hydroxyl radical oxidation processes in laboratory  
451 studies. *Atmospheric Environment*. 205, 9-18. <https://doi.org/10.1016/j.atmosenv.2019.02.039>, 2019.

452 Fleming, L. T., Ali, N. N., Blair, S. L., Roveretto, M., George, C., Nizkorodov, S. A.: Formation of Light-  
453 Absorbing Organosulfates during Evaporation of Secondary Organic Material Extracts in the Presence of Sulfuric  
454 Acid. *ACS Earth and Space Chemistry*. 3, 947-957. <https://doi.org/10.1021/acsearthspacechem.9b00036>, 2019.

455 Fleming, L. T., Lin, P., Roberts, J. M., Selimovic, V., Yokelson, R., Laskin, J., Laskin, A., Nizkorodov, S. A.:  
456 Molecular composition and photochemical lifetimes of brown carbon chromophores in biomass burning organic  
457 aerosol. *Atmospheric Chemistry and Physics*. 20, 1105-1129. <https://doi.org/10.5194/acp-20-1105-2020>, 2020.

458 Fu, T.-M., Jacob, D. J., Wittrock, F., Burrows, J. P., Vrekoussis, M., Henze, D. K.: Global budgets of atmospheric  
459 glyoxal and methylglyoxal, and implications for formation of secondary organic aerosols. *Journal of Geophysical*  
460 *Research: Atmospheres*. 113. <https://doi.org/10.1029/2007JD009505>, 2008.

461 Gao, Y., Zhang, Y.: Optical properties investigation of the reactions between methylglyoxal and  
462 glycine/ammonium sulfate. *Spectrochimica Acta Part A: Molecular and Biomolecular Spectroscopy*. 215, 112-121.  
463 <https://doi.org/10.1016/j.saa.2019.02.087>, 2019.

464 Gu, J., Dutta, S., Sioud, S., Go, B. R., Maity, B., Cavallo, L., Zhang, R., Chan, C. K.: Photoinduced  
465 Transformation in Glyoxal- and Methylglyoxal-Ammonium Solutions: Role of Photolysis and Photosensitization.  
466 *Environmental Science & Technology*. 59, 16628-16640. <https://doi.org/10.1021/acs.est.5c04889>, 2025.

467 Heald, C. L., Ridley, D. A., Kroll, J. H., Barrett, S. R. H., Cady-Pereira, K. E., Alvarado, M. J., Holmes, C. D.:  
468 Contrasting the direct radiative effect and direct radiative forcing of aerosols. *Atmospheric Chemistry and Physics*. 14,  
469 5513-5527. <https://doi.org/10.5194/acp-14-5513-2014>, 2014.

470 Hems, R. F., Abbatt, J. P. D.: Aqueous Phase Photo-oxidation of Brown Carbon Nitrophenols: Reaction Kinetics,  
471 Mechanism, and Evolution of Light Absorption. *ACS Earth and Space Chemistry*. 2, 225-234.  
472 <https://doi.org/10.1021/acsearthspacechem.7b00123>, 2018.

473 Hems, R. F., Schnitzler, E. G., Bastawrous, M., Soong, R., Simpson, A. J., Abbatt, J. P. D.: Aqueous  
474 Photoreactions of Wood Smoke Brown Carbon. *ACS Earth and Space Chemistry*. 4, 1149-1160.  
475 <https://doi.org/10.1021/acsearthspacechem.0c00117>, 2020.

476 Hems, R. F., Schnitzler, E. G., Liu-Kang, C., Cappa, C. D., Abbatt, J. P. D.: Aging of Atmospheric Brown Carbon  
477 Aerosol. *ACS Earth and Space Chemistry*. 5, 722-748. <https://doi.org/10.1021/acsearthspacechem.0c00346>, 2021.

478 Hurteau, M. D., Westerling, A. L., Wiedinmyer, C., Bryant, B. P.: Projected Effects of Climate and Development  
479 on California Wildfire Emissions through 2100. *Environmental Science & Technology*. 48, 2298-2304.  
480 <https://doi.org/10.1021/es4050133>, 2014.

481 Jain, P., Castellanos-Acuna, D., Coogan, S. C. P., Abatzoglou, J. T., Flannigan, M. D.: Observed increases in  
482 extreme fire weather driven by atmospheric humidity and temperature. *Nature Climate Change*. 12, 63-70.  
483 <https://doi.org/10.1038/s41558-021-01224-1>, 2022.

484 Jo, D. S., Park, R. J., Lee, S., Kim, S. W., Zhang, X.: A global simulation of brown carbon: implications for  
485 photochemistry and direct radiative effect. *Atmospheric Chemistry and Physics*. 16, 3413-3432.  
486 <https://doi.org/10.5194/acp-16-3413-2016>, 2016.

487 Kirchstetter, T. W., Novakov, T., Hobbs, P. V.: Evidence that the spectral dependence of light absorption by  
488 aerosols is affected by organic carbon. *Journal of Geophysical Research: Atmospheres*. 109.  
489 <https://doi.org/10.1029/2004JD004999>, 2004.

490 Laskin, A., Laskin, J., Nizkorodov, S. A.: Chemistry of Atmospheric Brown Carbon. *Chemical Reviews*. 115,  
491 4335-4382. <https://doi.org/10.1021/cr5006167>, 2015.

492 Li, Y., Fu, T.-M., Yu, J. Z., Zhang, A., Yu, X., Ye, J., Zhu, L., Shen, H., Wang, C., Yang, X., Tao, S., Chen, Q., Li,  
493 Y., Li, L., Che, H., Heald, C. L.: Nitrogen dominates global atmospheric organic aerosol absorption. *Science*. 387,  
494 989-995. <https://doi.org/10.1126/science.adr4473>, 2025.

495 Lin, P., Huang, X.-F., He, L.-Y., Zhen Yu, J.: Abundance and size distribution of HULIS in ambient aerosols at a  
496 rural site in South China. *Journal of Aerosol Science*. 41, 74-87. <https://doi.org/10.1016/j.jaerosci.2009.09.001>, 2010.

497 Lin, P., Bluvshstein, N., Rudich, Y., Nizkorodov, S. A., Laskin, J., Laskin, A.: Molecular Chemistry of  
498 Atmospheric Brown Carbon Inferred from a Nationwide Biomass Burning Event. *Environmental Science &*  
499 *Technology*. 51, 11561-11570. <https://doi.org/10.1021/acs.est.7b02276>, 2017.

500 Liu-Kang, C., Gallimore, P. J., Liu, T., Abbatt, J. P. D.: Photoreaction of biomass burning brown carbon aerosol  
501 particles. *Environmental Science: Atmospheres*. 2, 270-278. <https://doi.org/10.1039/d1ea00088h>, 2022.

502 Liu, D., He, C., Schwarz, J. P., Wang, X.: Lifecycle of light-absorbing carbonaceous aerosols in the atmosphere.  
503 npj Climate and Atmospheric Science. 3, 40. <https://doi.org/10.1038/s41612-020-00145-8>, 2020.

504 Liu, Y., Huang, R.-J., Lin, C., Yuan, W., Li, Y. J., Zhong, H., Yang, L., Wang, T., Huang, W., Xu, W., Huang, D.  
505 D., Huang, C.: Nitrate-Photolysis Shortens the Lifetimes of Brown Carbon Tracers from Biomass Burning.  
506 Environmental Science & Technology. 59, 640-649. <https://doi.org/10.1021/acs.est.4c06123>, 2025.

507 Magalhães, A. C. O., Esteves da Silva, J. C. G., Pinto da Silva, L.: Density Functional Theory Calculation of the  
508 Absorption Properties of Brown Carbon Chromophores Generated by Catechol Heterogeneous Ozonolysis. ACS Earth  
509 and Space Chemistry. 1, 353-360. <https://doi.org/10.1021/acsearthspacechem.7b00061>, 2017.

510 Müller, S., Giorio, C., Borduas-Dedekind, N.: Tracking the Photomineralization Mechanism in Irradiated Lab-  
511 Generated and Field-Collected Brown Carbon Samples and Its Effect on Cloud Condensation Nuclei Abilities. ACS  
512 Environmental Au. 3, 164-178. <https://doi.org/10.1021/acsenvironau.2c00055>, 2023.

513 Qiu, Y., Qiu, T., Wu, Z., Liu, Y., Fang, W., Man, R., Liu, Y., Wang, J., Meng, X., Chen, J., Liang, D., Guo, S., Hu,  
514 M.: Observational Evidence of Brown Carbon Photobleaching in Urban Atmosphere at Molecular Level.  
515 Environmental Science and Technology Letters. 11, 1032-1039. <https://doi.org/10.1021/acs.estlett.4c00647>, 2024.

516 Saleh, R., Marks, M., Heo, J., Adams, P. J., Donahue, N. M., Robinson, A. L.: Contribution of brown carbon and  
517 lensing to the direct radiative effect of carbonaceous aerosols from biomass and biofuel burning emissions. Journal of  
518 Geophysical Research: Atmospheres. 120, 2102-2110. <https://doi.org/10.1002/2015JD023697>, 2015.

519 Saleh, R.: From Measurements to Models: Toward Accurate Representation of Brown Carbon in Climate  
520 Calculations. Current Pollution Reports. 6, 90-104. <https://doi.org/10.1007/s40726-020-00139-3>, 2020.

521 Schnitzler, E. G., Abbatt, J. P. D.: Heterogeneous OH oxidation of secondary brown carbon aerosol. Atmospheric  
522 Chemistry and Physics. 18, 14539-14553. <https://doi.org/10.5194/acp-18-14539-2018>, 2018.

523 Schnitzler, E. G., Gerrebos, N. G. A., Carter, T. S., Huang, Y., Heald, C. L., Bertram, A. K., Abbatt, J. P. D.: Rate  
524 of atmospheric brown carbon whitening governed by environmental conditions. Proceedings of the National Academy  
525 of Sciences. 119, e2205610119. <https://doi.org/10.1073/pnas.2205610119>, 2022.

526 Shan, M., Carter, E., Baumgartner, J., Deng, M., Clark, S., Schauer, J. J., Ezzati, M., Li, J., Fu, Y., Yang, X.: A  
527 user-centered, iterative engineering approach for advanced biomass cookstove design and development. Environ. Res.  
528 Lett. 12, 095009. [10.1088/1748-9326/aa804f](https://doi.org/10.1088/1748-9326/aa804f), 2017.

529 Shen, Y., Pokhrel, R. P., Sullivan, A. P., Levin, E. J. T., Garofalo, L. A., Farmer, D. K., Permar, W., Hu, L., Toohey,  
530 D. W., Campos, T., Fischer, E. V., Murphy, S. M.: Understanding the mechanism and importance of brown carbon  
531 bleaching across the visible spectrum in biomass burning plumes from the WE-CAN campaign. Atmospheric  
532 Chemistry and Physics. 24, 12881-12901. <https://doi.org/10.5194/acp-24-12881-2024>, 2024.

533 Wang, Q., Zhou, Y., Ma, N., Zhu, Y., Zhao, X., Zhu, S., Tao, J., Hong, J., Wu, W., Cheng, Y., Su, H.: Review of  
534 Brown Carbon Aerosols in China: Pollution Level, Optical Properties, and Emissions. Journal of Geophysical  
535 Research: Atmospheres. 127, e2021JD035473. <https://doi.org/10.1029/2021JD035473>, 2022.

536 Wang, X., Heald, C. L., Ridley, D. A., Schwarz, J. P., Spackman, J. R., Perring, A. E., Coe, H., Liu, D., Clarke,

537 A. D.: Exploiting simultaneous observational constraints on mass and absorption to estimate the global direct radiative  
538 forcing of black carbon and brown carbon. *Atmospheric Chemistry and Physics*. 14, 10989-11010.  
539 <https://doi.org/10.5194/acp-14-10989-2014>, 2014.

540 Wang, X., Heald, C. L., Liu, J., Weber, R. J., Campuzano-Jost, P., Jimenez, J. L., Schwarz, J. P., Perring, A. E.:  
541 Exploring the observational constraints on the simulation of brown carbon. *Atmospheric Chemistry and Physics*. 18,  
542 635-653. <https://doi.org/10.5194/acp-18-635-2018>, 2018.

543 Wang, X., Chakrabarty, R. K., Schwarz, J. P., Murphy, S. M., Levin, E. J. T., Howell, S. G., Guo, H., Campuzano-  
544 Jost, P., Jimenez, J. L.: Dark brown carbon from biomass burning contributes to significant global-scale positive  
545 forcing. *One Earth*. 8, 101205. <https://doi.org/10.1016/j.oneear.2025.101205>, 2025.

546 Wang, Y., Hu, M., Lin, P., Guo, Q., Wu, Z., Li, M., Zeng, L., Song, Y., Zeng, L., Wu, Y., Guo, S., Huang, X., He,  
547 L.: Molecular Characterization of Nitrogen-Containing Organic Compounds in Humic-like Substances Emitted from  
548 Straw Residue Burning. *Environmental Science & Technology*. 51, 5951-5961.  
549 <https://doi.org/10.1021/acs.est.7b00248>, 2017.

550 Wang, Y., Hu, M., Lin, P., Tan, T., Li, M., Xu, N., Zheng, J., Du, Z., Qin, Y., Wu, Y., Lu, S., Song, Y., Wu, Z.,  
551 Guo, S., Zeng, L., Huang, X., He, L.: Enhancement in Particulate Organic Nitrogen and Light Absorption of Humic-  
552 Like Substances over Tibetan Plateau Due to Long-Range Transported Biomass Burning Emissions. *Environmental*  
553 *Science & Technology*. 53, 14222-14232. <https://doi.org/10.1021/acs.est.9b06152>, 2019.

554 Wong, J. P. S., Tsagkaraki, M., Tsiodra, I., Mihalopoulos, N., Violaki, K., Kanakidou, M., Sciare, J., Nenes, A.,  
555 Weber, R. J.: Atmospheric evolution of molecular-weight-separated brown carbon from biomass burning. *Atmospheric*  
556 *Chemistry and Physics*. 19, 7319-7334. <https://doi.org/10.5194/acp-19-7319-2019>, 2019.

557 Xiong, R., Li, J., Zhang, Y., Zhang, L., Jiang, K., Zheng, H., Kong, S., Shen, H., Cheng, H., Shen, G., Tao, S.:  
558 Global brown carbon emissions from combustion sources. *Environmental Science and Ecotechnology*. 12, 100201.  
559 <https://doi.org/10.1016/j.ese.2022.100201>, 2022.

560 Xu, L., Lin, G., Liu, X., Wu, C., Wu, Y., Lou, S.: Constraining Light Absorption of Brown Carbon in China and  
561 Implications for Aerosol Direct Radiative Effect. *Geophysical Research Letters*. 51, e2024GL109861.  
562 <https://doi.org/10.1029/2024GL109861>, 2024.

563 Yang, L., Huang, R.-J., Yuan, W., Huang, D. D., Huang, C.: pH-Dependent Aqueous-Phase Brown Carbon  
564 Formation: Rate Constants and Implications for Solar Absorption and Atmospheric Photochemistry. *Environmental*  
565 *Science & Technology*, 1236-1243. <https://doi.org/10.1021/acs.est.3c07631>, 2024.

566 Yue, S., Zhu, J., Chen, S., Xie, Q., Li, W., Li, L., Ren, H., Su, S., Li, P., Ma, H., Fan, Y., Cheng, B., Wu, L., Deng,  
567 J., Hu, W., Ren, L., Wei, L., Zhao, W., Tian, Y., Pan, X., Sun, Y., Wang, Z., Wu, F., Liu, C.-Q., Su, H., Penner, J. E.,  
568 Pöschl, U., Andreae, M. O., Cheng, Y., Fu, P.: Brown carbon from biomass burning imposes strong circum-Arctic  
569 warming. *One Earth*. 5, 293-304. <https://doi.org/10.1016/j.oneear.2022.02.006>, 2022.

570 Yue, X., Mickley, L. J., Logan, J. A., Kaplan, J. O.: Ensemble projections of wildfire activity and carbonaceous  
571 aerosol concentrations over the western United States in the mid-21st century. *Atmospheric Environment*. 77, 767-  
572 780. <https://doi.org/10.1016/j.atmosenv.2013.06.003>, 2013.

573 Zeng, L., Zhang, A., Wang, Y., Wagner, N. L., Katich, J. M., Schwarz, J. P., Schill, G. P., Brock, C., Froyd, K. D.,  
574 Murphy, D. M., Williamson, C. J., Kupc, A., Scheuer, E., Dibb, J., Weber, R. J.: Global Measurements of Brown  
575 Carbon and Estimated Direct Radiative Effects. *Geophysical Research Letters*. 47, e2020GL088747.  
576 <https://doi.org/10.1029/2020GL088747>, 2020.

577 Zeng, Y., Ning, Y., Shen, Z., Zhang, L., Zhang, T., Lei, Y., Zhang, Q., Li, G., Xu, H., Ho, S. S. H., Cao, J.: The  
578 Roles of N, S, and O in Molecular Absorption Features of Brown Carbon in PM<sub>2.5</sub> in a Typical Semi-Arid Megacity  
579 in Northwestern China. *Journal of Geophysical Research: Atmospheres*. 126, e2021JD034791.  
580 <https://doi.org/10.1029/2021JD034791>, 2021.

581 Zhang, Q., Wang, Y., Xiao, Q., Geng, G., Davis, S. J., Liu, X., Yang, J., Liu, J., Huang, W., He, C., Luo, B.,  
582 Martin, R. V., Brauer, M., Randerson, J. T., He, K.: Long-range PM<sub>2.5</sub> pollution and health impacts from the 2023  
583 Canadian wildfires. *Nature*. <https://doi.org/10.1038/s41586-025-09482-1>, 2025.

584 Zhang, X., Chen, S., Kang, L., Yuan, T., Luo, Y., Alam, K., Li, J., He, Y., Bi, H., Zhao, D.: Direct Radiative  
585 Forcing Induced by Light-Absorbing Aerosols in Different Climate Regions Over East Asia. *Journal of Geophysical  
586 Research: Atmospheres*. 125, e2019JD032228. <https://doi.org/10.1029/2019JD032228>, 2020.

587 Zhao, R., Mungall, E. L., Lee, A. K. Y., Aljawhary, D., Abbatt, J. P. D.: Aqueous-phase photooxidation of  
588 levoglucosan &ndash; a mechanistic study using aerosol time-of-flight chemical ionization mass spectrometry  
589 (Aerosol ToF-CIMS). *Atmospheric Chemistry and Physics*. 14, 9695-9706. <https://doi.org/10.5194/acp-14-9695-2014>,  
590 2014.

591 Zhao, R., Lee, A. K. Y., Huang, L., Li, X., Yang, F., Abbatt, J. P. D.: Photochemical processing of aqueous  
592 atmospheric brown carbon. *Atmospheric Chemistry and Physics*. 15, 6087-6100. [https://doi.org/10.5194/acp-15-6087-  
593 2015](https://doi.org/10.5194/acp-15-6087-2015), 2015.

594